Structural Engineering and Mechanics, *Vol. 65, No. 3 (2018) 291-302*
DOI: https://doi.org/10.12989/sem.2018.65.3.291

A 3-D RBSM for simulating the failure process of RC structures

Xingu Zhong[1, 2a], Chao Zhao*[2], Bo Liu[2, 3a], Xiaojuan Shu[1a] and Mingyan Shen[1a]

[1]*School of Civil Engineering, Hunan University of Science and Technology, Taoyuan Road, Yuhu District, Xiangtan, China*
[2]*School of Mechanics and Civil Engineering, China University of Mining and Technology (Beijing), Ding No.11 Xueyuan Road, Haidian District, Beijing, China*
[3]*State Key Laboratory of Deep Geomechanics and Underground Engineering, No.16 Qinghua East Road, Haidian District, Beijing, China*

(Received September 12, 2017, Revised November 23, 2017, Accepted December 8, 2017)

Abstract. Rigid body spring method (RBSM) is an effective tool to simulate the cracking process of structures, and has been successfully applied to investigate the behavior of reinforced concrete (RC) members. However, the theoretical researches and engineering applications of this method mainly focus on two-dimensional problems as yet, which greatly limits its applications in actual engineering projects. In this study, a three-dimensional (3-D) RBSM for RC structures is proposed. In the proposed model, concrete, reinforcing steels, and their interfaces are represented as discrete entities. Concrete is partitioned into a collection of rigid blocks and a uniform distribution of normal and tangential springs is defined along their boundaries to reflect its material properties. Reinforcement is modeled as a series of bar elements which can be freely positioned in the structural domain and irrespective of the mesh geometry of concrete. The bond-slip characteristics between reinforcing steel and concrete are also considered by introducing special linkage elements. The applicability and effectiveness of the proposed method is firstly confirmed by an elastic T-shape beam, and then it is applied to analyze the failure processes of a Z-type component under direct shear loading and a RC beam under two-point loading.

Keywords: reinforced concrete structures; failure process; rigid body spring model; cracks; simplex integration

1. Introduction

The failure process of a RC structure is often accompanied with the generation and propagation of cracks. Cracks not only induce discontinuity in the medium but also cause stress redistribution and stiffness degradation in regions around cracks, which makes the failure process analysis of RC structures a complicated and difficult task.

Finite element method (FEM) is the main method used in the failure process analysis of RC structures, in which two measures are often adopted to deal with cracks. One measure is to regard cracks as boundaries of elements (Carter *et al*. 2000), which must update the element mesh with the propagation of cracks to ensure that cracks are always on the boundaries of elements. The other measure is to smear cracks into elements, and the effect of cracks is taken into consideration by adjusting element stiffness matrixes or material constitutive relations (Hariri-Ardebili and Seyed-Kolbadi 2015, Ors *et al*. 2016, Kara *et al*. 2017, Murthy and Priya 2017). This measure can avoid updating the element mesh but fails to provide the characteristics of the cracks, such as the profile and the position. Belytschko *et al*. (Belytschko and Black 1999, Jiang and Du 2017, Nanda Kumar *et al*. 2017) proposed a modified FEM named the Extended Finite Element Method to analyze the propagation process of cracks, in which the step function and the enrichment function are introduced to describe the discontinuous displacements around cracks. This measure has the advantages of the above two but cannot work with the phenomenon of multidirectional cracking.

In recent years, numerical methods based on discrete mechanics have been proposed and widely applied to rock and concrete structures (Shi 1988, 1994, Li *et al*. 2015, Guo and Zhao 2014, Burns and Hanley 2017). The discrete methods do not rely on the continuum assumption which makes it an efficient and convenient tool to simulate the cracking process of structures. The rigid body spring method (RSBM) is one such method which was firstly proposed by Kawai (1977). RBSM can show realistic behavior from cracking to failure (Yao *et al*. 2015, Yao *et al*. 2017, Gu *et al*. 2013, Zhang *et al*. 2012, Zhang 1999), and has been successfully applied to investigate the behavior of reinforced concrete (RC) members and prestressed concrete members (Bolander and Saito 1998, Saito and Hikosaka 1999, Bolander *et al*. 2000). However, the theoretical researches and engineering applications of this method mainly focus on two-dimensional problems as yet, which greatly limit its applications in actual engineering projects. In this study, a 3-D RBSM for simulating the failure process of reinforced concrete structures is proposed.

In the proposed model, concrete, reinforcing steels, and their interface are represented as discrete entities. Concrete

*Corresponding author, Ph.D. Student
E-mail: 287832614@qq.com
[a]Ph.D.
[b]Ph.D. Student

ISSN: 1225-4568 (Print), 1598-6217 (Online)

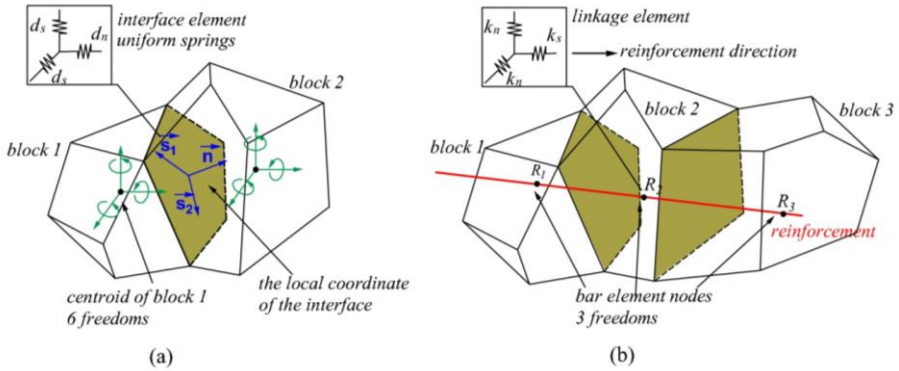

Fig. 1 a rigid body spring model for RC structures: (a) concrete model; (b) reinforcement and bond-slip modeling

is partitioned into a collection of rigid blocks, and a uniform distribution of normal and tangential springs along their boundaries is defined to reflect the material properties of concrete, as shown in Fig. 1(a). Reinforcement is modeled as a series of bar element that can be freely positioned in the structural domain and irrespective of the mesh geometry of concrete. The bond-slip characteristics between reinforcing steel and concrete are also considered by introducing special linkage elements that are placed along the reinforcement-concrete interface, as shown in Fig. 1(b). Numerical integration on complex polyhedrons and polygons is the key problem of three-dimensional RBSM, and an efficient and accurate integral method is proposed in this paper. The effectiveness and applicability of the proposed method is firstly verified through the analyses of an elastic cantilever T-shape beam under two different load conditions, and then it is applied to analyze the failure processes of a Z-type component under direct shear loading and a RC beam under two-point loading.

2. Concrete model

2.1 Basic displacements of blocks

In this study, the rigid blocks used to represent concrete may be arbitrary three-dimension convex polyhedrons, and there are six degrees of freedom (DOF) defined at the centroid of each block, three translational DOFs and three rotational DOFs, as shown in Fig. 2. The displacements of an arbitrary point on a block are completely controlled by centriodal freedoms of the block, the mathematical expression is as follows,

$$\mathbf{u} = \begin{bmatrix} u & v & w \end{bmatrix}^{\mathrm{T}} = \mathbf{N} \bullet \mathbf{u_g} \tag{1}$$

$$\mathbf{N} = \begin{bmatrix} 1 & 0 & 0 & 0 & (z-z_g) & (y-y_g) \\ 0 & 1 & 0 & (z_g-z) & 0 & (x-x_g) \\ 0 & 0 & 1 & (y-y_g) & (x_g-x) & 0 \end{bmatrix} \tag{2}$$

$$\mathbf{u_g} = \begin{bmatrix} u_g & v_g & w_g & \theta_x & \theta_y & \theta_z \end{bmatrix}^{\mathrm{T}} \tag{3}$$

where u, v, w are the translation displacements of a point on the block, respectively; $\mathbf{N}$, $\boldsymbol{u_g}$ are the shape function matrix and the centroidal displacements of the block, respectively; u_g, v_g, w_g, θ_x, θ_y, θ_z are the translational displacements and the rotational displacement of the block respectively, as shown in Fig. 2; x, y, z are the global coordinates of an arbitrary point on the block; x_g, y_g, z_g are the global coordinates of the centroid.

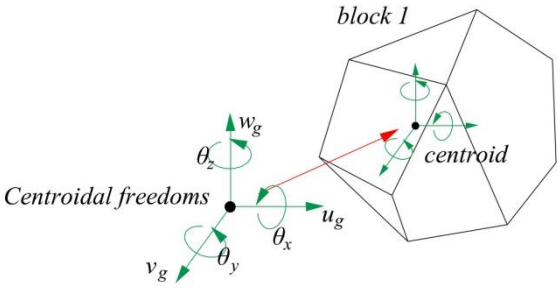

Fig. 2 Centriodal freedoms of blocks

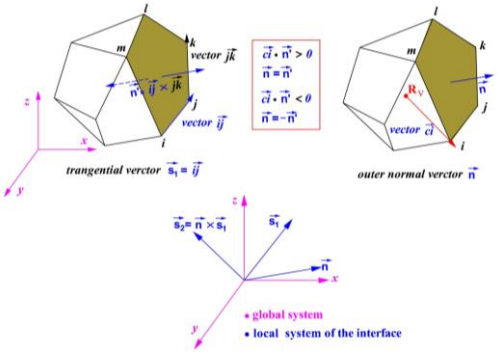

Fig. 3 Local system for interface elements

2.2 Spring deformation and spring force of interfaces

Interface elements can be generated by checking the common vertexes of any two blocks in rigid body spring models. If there are three or more common vertexes between two blocks, there is an interface. Rather than using concentrating springs to reflect the properties of concrete in the initial RBSM (Bolander and Saito 1998, Saito and Hikosaka 1999, Bolander *et al.* 2000), a uniform distribution of normal and tangential springs is defined

along the boundaries of adjacent rigid blocks in this paper. Fig. 3 shows the corresponding relationship between the local system of interface elements and the global system, which is the premise to calcuate the sping deformation and force of interface elements. The local coordinate system consists of two tangential vectors ($\vec{s}_1, \vec{s}_2$) and an outer normal vector ($\vec{n}$), which can be established by the method as shown in Fig. 3.

Point R_v in Fig. 3 is defined as,

$$\begin{cases} x_{R_v} = \dfrac{x_1 + \cdots + x_i + \cdots + x_{m_{block}}}{m_{block}} \\ y_{R_v} = \dfrac{y_1 + \cdots + y_i + \cdots + y_{m_{block}}}{m_{block}} \\ z_{R_v} = \dfrac{z_1 + \cdots + z_i + \cdots + z_{m_{block}}}{m_{block}} \end{cases} \tag{4}$$

where m_{block} is the number of vertexes composing the rigid block, and x_i, y_i, z_i are their coordinates.

The spring deformation of an interface can be determined by the relative displacement between two neighbouring blocks,

$$\boldsymbol{\delta} = \begin{bmatrix} \delta_n & \delta_{s_1} & \delta_{s_2} \end{bmatrix}^{\mathrm{T}} = -\mathbf{L}(\mathbf{u}_1 - \mathbf{u}_2) \tag{5}$$

where δ_n, δ_{s_1}, δ_{s_2} are the relative displacements of one point on the block interface, respectively; $\mathbf{u}_1$ and $\mathbf{u}_2$ are the displacements of adjacent rigid blocks respectively, which are defined by Eq. (1); **L** is the coordinate-transformation matrix.

With the local system established in Fig. 3, **L** is given by

$$\mathbf{L} = \begin{bmatrix} \cos(\vec{\mathbf{n}}_1, \vec{\mathbf{x}}) & \cos(\vec{\mathbf{n}}_1, \vec{\mathbf{y}}) & \cos(\vec{\mathbf{n}}_1, \vec{\mathbf{z}}) \\ \cos(\vec{\mathbf{s}}_1, \vec{\mathbf{x}}) & \cos(\vec{\mathbf{s}}_1, \vec{\mathbf{y}}) & \cos(\vec{\mathbf{s}}_1, \vec{\mathbf{z}}) \\ \cos(\vec{\mathbf{s}}_2, \vec{\mathbf{x}}) & \cos(\vec{\mathbf{s}}_2, \vec{\mathbf{y}}) & \cos(\vec{\mathbf{s}}_2, \vec{\mathbf{z}}) \end{bmatrix} \tag{6}$$

The local spring forces **T** on the interface are related to the spring deformation $\boldsymbol{\delta}$ by the following constitutive relation

$$\mathbf{T} = \begin{bmatrix} \sigma_n & \tau_{s_1} & \tau_{s_2} \end{bmatrix}^{\mathrm{T}} = \mathbf{D}\boldsymbol{\delta} \tag{7}$$

where σ_n, τ_{s_1}, τ_{s_2} denote the normal and tangential spring forces of concrete, respectively; **D** is the matrix of interfacial spring stiffness,

$$\mathbf{D} = \begin{bmatrix} d_n & & \\ & d_s & \\ & & d_s \end{bmatrix}^{\mathrm{T}}$$

$$d_n = \frac{E(1-\lambda)}{(1-\lambda-\lambda^2)(h_1+h_2)} \tag{8}$$

$$d_s = \frac{E}{2(1+\lambda)(h_1+h_2)}$$

λ, E are Poisson's ratio and the elastic modulus of concrete, respectively; d_n and d_s are the stiffness of the normal and tangential springs, respectively; h_1 and h_2 are the vertical distances from the centroids of neighbouring blocks to their interface, respectively.

2.3 Virtual work equation

The overall energy balance equation is given as follows

$$\sum_r \iint_{S_0^r} \frac{1}{2}\mathbf{T}^{(i)}\boldsymbol{\delta}^{(i)} ds = \sum_e \iiint_{\Omega^e} f_i \mathbf{u}_\mathbf{i} d\Omega + \iint_{S_\sigma^e} \frac{1}{2}\mathbf{P}_\mathbf{i}\mathbf{u}_\mathbf{i} ds \tag{9}$$

where Ω^e is the domain of definition; S_σ^e is the force boundary; S_0^r is an interface in the domain; f_i, $\mathbf{P_i}$ are the gravity density of the material and the imposed loads, respectively. (Note: throughout the article, superscript i means the number of interfaces and subscript i means the number of blocks.)

After applying the principle of stationary potential energy, the following equilibrium equation is obtained

$$\mathbf{K} \cdot \mathbf{U}_\mathbf{g} = \mathbf{R} \tag{10}$$

where **K** is the global stiffness matrix of the model; **R** is the equivalent nodal load array of the model; $\mathbf{U_g}$ is the global displacement array of the model.

2.4 Material model for concrete

Penetration and separation between two blocks are allowed in the proposed model, which can be used to reflect the compressive strain and tensile strain of concrete, respectively. Stiffnesses of springs defined along interfaces reflect the ability of concrete to resist penetration and separation between two blocks, which can be adjusted according to current stress states of interfaces to simulate the nonlinearity of concrete.

2.4.1 Concrete model under compression

In this study, the concrete under compression shows the nonlinear behaviour up to the compressive strength and after the peak a softening branch exists until failure, as shown in Fig. 4(a), which is idealized as the following equations (Saito and Hikosaka 1999).

$$\sigma = \begin{cases} E_0\varepsilon - \dfrac{E_0}{2\varepsilon_0}\varepsilon^2 & (\varepsilon < \varepsilon_0) \\ f_c - \dfrac{(f_c - \mu f_c)}{(\varepsilon_{cu} - \varepsilon_0)}(\varepsilon - \varepsilon_0) & (\varepsilon_0 \le \varepsilon < \varepsilon_{cu}) \\ \mu f_c & (\varepsilon > \varepsilon_{cu}) \end{cases} \tag{11}$$

where $\varepsilon = \delta_n/(h_1+h_2)$; E_0 is the initial modulus of elasticity; f_c is the compressive strength, and $\varepsilon_0 = 2f_c/E$. The ultimate strain ε_{cu} is set to 4 ε_0, and μ is set to 0.2 in this study.

The secant modulus of concrete E is determined by the following equation,

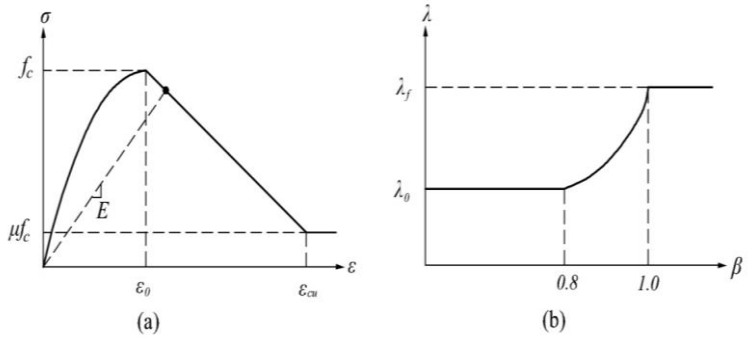

Fig. 4 Concrete model under compression: (a) compression model; (b) Poisson's ratio

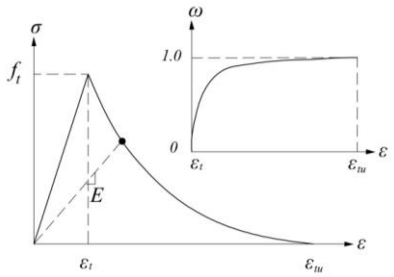

Fig. 5 Tension softening model for concrete

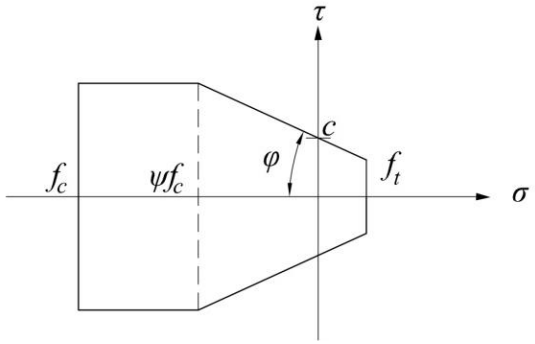

Fig. 6 Mohr-Coulomb criterion for shear spring

$$E = \sigma / \varepsilon \tag{12}$$

It has been experimentally observed that, in presence of compressive stresses, concrete tends firstly to compact and subsequently to expand after the appearance of micro cracks. To reproduce this behavior, the Poisson coefficient λ is expressed as function of the non-linearity index β and properly adjusted during the analysis according to Bernardi *et al*. (2015), as shown in Fig. 4(b). That is,

$$\begin{cases} \lambda = \lambda_0 & (\beta < \beta_a) \\ \lambda = \lambda_f - (\lambda_f - \lambda_0)\sqrt{1-\left(\dfrac{\beta-\beta_a}{1-\beta_a}\right)^2} & (\beta_a \le \beta < 1) \\ \lambda = \lambda_f & (\beta > 1) \end{cases} \tag{13}$$

where $\beta\ \varepsilon/\varepsilon_0$, and limit value β_a equal to 0.8; λ_0 indicates the initial value of Poisson coefficient (assumed equal to 0.2), while λ_f represents its secant value at peak (approximately equal to 0.36).

2.4.2 Concrete model under tension

Concrete under tension behaves linearly elastic up to the tensile strength, then the stress-strain relationship exhibits strain softening until failure, as shown in Fig. 5. By introducing the damage parameter ω, the tension softening curve is defined by (Saito and Hikosaka 1999)

$$\sigma = (1-\omega)E_0\varepsilon \tag{14}$$

where

$$\omega = \begin{cases} 0 & (\varepsilon \le \varepsilon_t) \\ 1-\dfrac{\varepsilon_t}{\varepsilon}\exp\left[-\dfrac{\kappa}{\varepsilon_{tu}}(\varepsilon-\varepsilon_t)\right] & (\varepsilon > \varepsilon_t) \end{cases} \tag{15}$$

in which ε is the normal strain of concrete, and $\varepsilon_t = f_t/E_0$; f_t is the tensile strength. The damage parameter ω represents the degree of damage and varies from 0 (no damage) up to 1 (complete damage). The constant parameter κ is set to 5. The ultimate strain ε_{tu} is calculated by the following equation,

$$\varepsilon_{tu} = \kappa\left(\frac{G_f}{f_t(h_1+h_2)} - \frac{f_t}{2E_0}\right) \tag{16}$$

where G_f is the fracture energy which represents the amount of energy consumed to create a crack of one-unit area; h_1 and h_2 are the vertical distances from the centroids of adjacent blocks to the interface.

The Poisson coefficient λ of concrete under tension is equal to λ_0 until the tensile stress reaches the tensile strength, after that it turns to λ_f.

2.4.3 Shear transferring model for concrete

Tangential springs represent the shear transferring mechanism of concrete. The shear strength is assumed to follow the Mohr-Coulomb type criterion with the tension and compression caps, as shown in Fig. 6. C and φ are the cohesion and internal friction angle, respectively. ψ is a constant parameter, and is set to 0.5. The shear fracture criterion is therefore expressed as (Saito and Hikosaka 1999),

$$\frac{\tau_{s_1}^2 + \tau_{s_2}^2}{\tau_f^2} \ge 1 \tag{17}$$

where

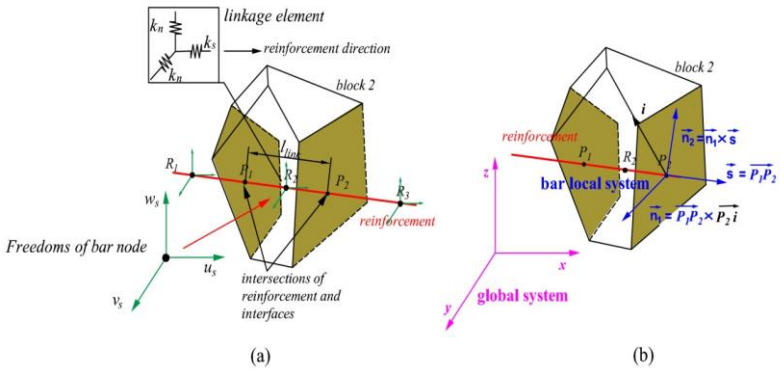

Fig. 7 Linkage element between concrete and reinforcement: (a) linkage element; (b) corresponding local ststem

$$\tau_f = \begin{cases} c - \sigma \tan\varphi & (\sigma \geq \psi f_c) \\ c - \psi f_c \tan\varphi & (\sigma < \psi f_c) \end{cases} \tag{18}$$

When the tangential spring reaches the strength τ_f, cracks occur. There are two failure modes: the tensile-shear failure ($\tau^2/\tau_f^2 \geq 1, \sigma \geq 0$) and the compression-shear failure ($\tau^2/\tau_f^2 \geq 1, \sigma < 0$).

For the compression-shear failure, the original interface spring matrix Eq. (8) is replaced by

$$\mathbf{D} = \begin{bmatrix} d_n & & \\ & \chi d_s & \\ & & \chi d_s \end{bmatrix}^{\mathrm{T}} \tag{19}$$

where χ is a reduction coefficient of the spring stiffness d_s, which is used to consider the aggregate interlock of concrete.

For the tensile-shear failure, the original interface spring matrix Eq. (8) is replaced by

$$\mathbf{D} = \begin{bmatrix} 0 & & \\ & \chi d_s & \\ & & \chi d_s \end{bmatrix}^{\mathrm{T}} \tag{20}$$

The method proposed by Wang *et al*. (2002) is adopted to consider the contribution of aggregate interlock,

$$\begin{aligned} \chi &= 1 && (\varepsilon < \varepsilon_t) \\ \chi &= 0.4/(\varepsilon/\varepsilon_t) && (\varepsilon \geq \varepsilon_t) \end{aligned} \tag{21}$$

where ε_t is the tensile strain of concrete corresponding to the tensile strength f_t.

3. Reinforcement model

Reinforcement is modelled as a series of bar element that can be freely positioned in the structural domain and irrespective of the mesh geometry of concrete. The bond-slip characteristics between reinforcing steel and concrete are also considered by introducing special linkage elements that are placed along the reinforcement-concrete interface, as shown in Fig. 7(a). Considering that the bar element model has been widely used in numerical simulations, the emphasis of this section is put on the linkage elements.

3.1 Discrete modeling of reinforcement

Reinforcement is represented by a series of regular bar elements. Each node of a bar element has three translation freedoms (u_s, v_s, w_s) and are attached to the concrete rigid blocks through zero-length link elements. Assuming small displacements occur, the displacements $\mathbf{u}_c$ at the point $P_2(x_2, y_2, z_2)$ located on block 2 in Fig. 7(a) is determined by Eq. (1). Thus, the relative displacements (or slippages) between concrete and steel bars are expressed by,

$$\boldsymbol{\delta}_s' = \begin{bmatrix} \delta_s' & \delta_{n1}' & \delta_{n2}' \end{bmatrix} = (\mathbf{u}_c - \mathbf{u}_s) = \mathbf{N}_s \mathbf{u}_s \tag{22}$$

$$\mathbf{u}_s = \begin{bmatrix} u_g & v_g & w_g & \theta_x & \theta_y & \theta_z & u_s & v_s & w_s \end{bmatrix}^{\mathrm{T}} \tag{23}$$

$$\mathbf{N}_s = \begin{bmatrix} 1 & 0 & 0 & 0 & (z_2 - z_g) & (y_g - y_2) & -1 & 0 & 0 \\ 0 & 1 & 0 & (z_g - z_2) & 0 & (x_2 - x_g) & 0 & -1 & 0 \\ 0 & 0 & 1 & (y_2 - y_g) & (x_g - x_2) & 0 & 0 & 0 & -1 \end{bmatrix} \tag{24}$$

where δ_s', δ_{n1}', δ_{n2}' are the relative displacements (or slippages) between concrete and steel bars.

To obtain the local displacement $\boldsymbol{\delta}_s$, it is necessary to use an appropriate coordinate transformation matrix $\mathbf{T}$. That is

$$\boldsymbol{\delta}_s = \begin{bmatrix} \delta_s & \delta_{n1} & \delta_{n2} \end{bmatrix} = \mathbf{T} \boldsymbol{\delta}_s' \tag{25}$$

With the bar local system established in Fig. 7(b), $\mathbf{T}$ is given by

$$\mathbf{T} = \begin{bmatrix} \cos(\vec{s}, \vec{\mathbf{x}}) & \cos(\vec{s}, \vec{\mathbf{y}}) & \cos(\vec{s}, \vec{\mathbf{z}}) \\ \cos(\vec{n}_1, \vec{\mathbf{x}}) & \cos(\vec{n}_1, \vec{\mathbf{y}}) & \cos(\vec{s}, \vec{\mathbf{z}}) \\ \cos(\vec{n}_2, \vec{\mathbf{x}}) & \cos(\vec{n}_2, \vec{\mathbf{y}}) & \cos(\vec{n}_2, \vec{\mathbf{z}}) \end{bmatrix} \tag{26}$$

After applying the principle of stationary potential energy, the element local stiffness matrix for the linkage element can be written as follows,

$$\mathbf{K}_s = \mathbf{N}_s^{\mathrm{T}} \mathbf{T}^{\mathrm{T}} \mathbf{D}_s \mathbf{T} \mathbf{N}_s \tag{27}$$

where,

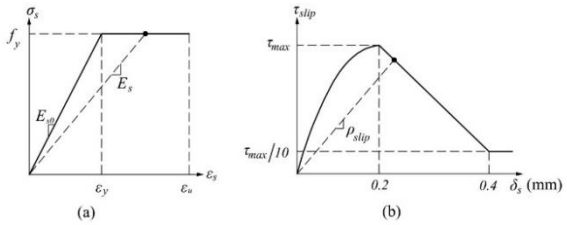

Fig. 8 Material model for reinforcement: (a) stress-strain relation for reinforcing steel; (b) idealization of bond stress-slip relationship

$$\mathbf{D_s}=\begin{bmatrix} k_s & 0 & 0 \\ 0 & k_n & 0 \\ 0 & 0 & k_n \end{bmatrix} \begin{matrix} k_s = l_{link} S_{surface} \rho_{slip} \\ k_n = \infty \end{matrix} \tag{28}$$

k_s, k_n are the tangential and normal spring stiffnesses of the linkage element, respectively; l_{link} is the computational length of the linkage element, as shown in Fig. 7(a); $S_{surface}$ is the surface area of a steel bar; ρ_{slip} is the slip coefficient between concrete and steel bars. k_n is set to a large value since the relative displacements normal to the steel bar direction are not expected.

3.2 Material model for reinforcement

Material stress-strain relation for steel reinforcing bars is idealized as a bilinear curve as shown in Fig. 8(a). The secant modulus of reinforcement E_s is determined by the function of reinforcement strain,

$$E_s=\frac{\sigma_s}{\varepsilon_s}=\begin{cases} E_{s0} & \varepsilon_s<\varepsilon_y \\ \dfrac{f_y}{\varepsilon_s}+\dfrac{(f_u-f_y)(\varepsilon_s-\varepsilon_y)}{\varepsilon_s(\varepsilon_u-\varepsilon_y)} & \varepsilon_y\le\varepsilon_s<\varepsilon_u \\ 0 & \varepsilon_s>\varepsilon_u \end{cases} \tag{29}$$

where σ_s and ε_s are the axial stress and axial strain of the steel bars, respectively; E_{s0} is the initial elastic modulus of reinforcement; f_y and ε_y are the yield tensile strength and strain of steel bars, respectively; f_u and ε_u are the ultimate tensile strength and strain of the steel bars, respectively.

The bond-slip interaction between concrete and steel bars strongly affects the crack condition and the stress in the reinforcement. The spring k_s in Eq. (28), parallel to the reinforcing bar, is defined to take account of the bond-slip interaction, and the slip coefficient ρ_{slip} can be represented as function of slippages between concrete and steel bars,

$$\rho_{slip}=\tau_{slip}/\delta_s \tag{30}$$

where δ_s represents the slippage (parallel to the reinforcing bar) between concrete and steel bars; τ_{slip} is the bond stress.

As shown in Fig. 8(b), the bond stress-slip relation adopted in this paper shows the nonlinear behavior up to peak strength (Gedik *et al*. 2011, Serhat and Metin 2015), which is defined by Eq. (31), and after the peak strength the curve proposed by Committee Euro-international Du Beton (1990) is assumed. That is

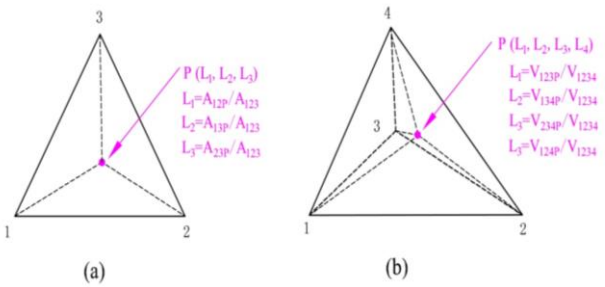

Fig. 9 Natural coordinate system adopted in simplex integration: (a) the area coordinate system for triangles; (b) the volume coordinate system for tetrahedron

$$\tau_{slip}=0.36 f_c^{2/3}\left\{1-\exp\left(-40(\delta_s/d_b)^{0.5}\right)\right\} \tag{31}$$

where d_b is diameter of the steel bar.

4. Numerical integration of 3-D RBSM

The numerical integration is needed when deriving elment stiffness matrixes of cocnrete and reinforcement. Considering that the integral domains in 3-D RBSM are usually complex polyhedrons or polygons, an efficient and accurate numerical integral method based on simplex integration method (Shi, 1994) is proposed. The simplex integration formulas are valid only when the integral region is a simplex, so complex integral domains need to be divided into simplexes. After that, applying simplex integration formula to each unit simplex, and then superposing the results.

4.1 Simplex integration method

The surface integral over a spatial triangle can be carried out according to the following equation,

$$\iint_{S_0^r} L_1^a L_2^b L_3^c dxdy=\frac{a!b!c!}{(a+b+c+2)!}2A_{1234} \tag{32}$$

where S_0^r is the integral domain; $L_i(i=1,2,3)$ are area coordinates of the triangle as shown in Fig. 9(a); A_{1234} is the area of the triangle.

The correspondence between the area coordinates L_i and the global coordinates (x, y, z) are given by the following equations,

$$\begin{cases} x=L_1x_1+L_2x_2+L_3x_3 \\ y=L_1y_1+L_2y_2+L_3y_3 \\ z=L_1z_1+L_2z_2+L_3z_3 \end{cases} \tag{33}$$

where x_i, y_i, z_i (i=1,2,3) are vertex coordinates of the triangle in global coordinate system.

The volume integration over a spatial tetrahedron can be carried out according to the following equation,

$$\iiint_{\Omega^e} L_1^a L_2^b L_3^c L_4^d dxdydz=\frac{a!b!c!d!}{(a+b+c+d+3)!}6V_{1234} \tag{34}$$

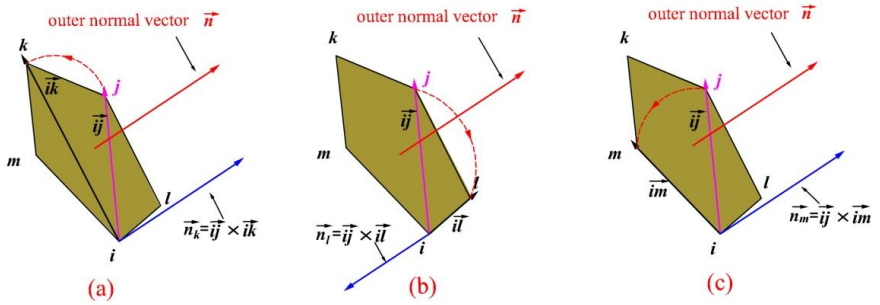

Fig. 10 Determination of the storage order of vertex *j*: (a) Relative position of vertex *j* and *k*; (b) Relative position of vertex *j* and *l*; (c) Relative position of vertex *j* and *m*

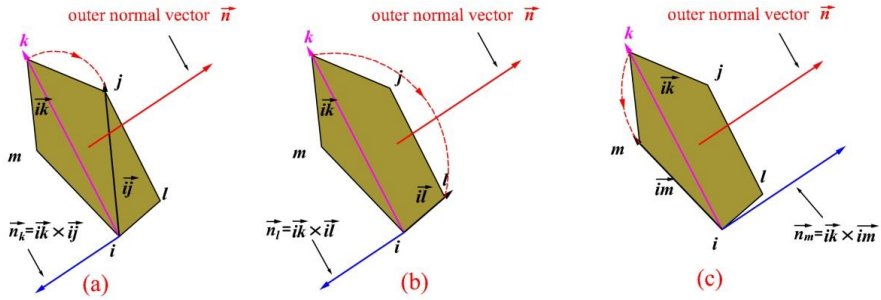

Fig. 11 Determination of the storage order of vertex *k*: (a) Relative position of vertex *k* and *j*; (b) Relative position of vertex *k* and *l*; (c) Relative position of vertex *k* and *m*

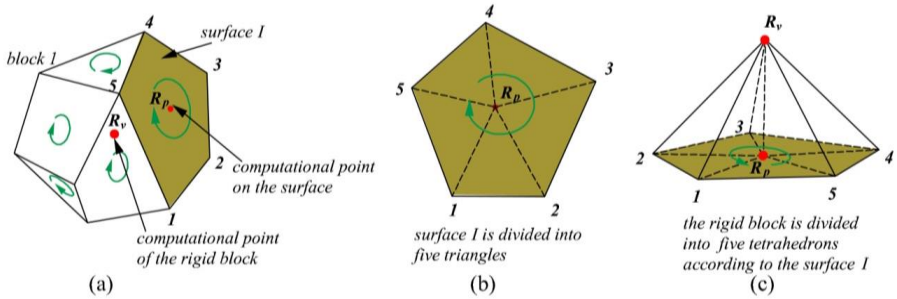

Fig. 12 The integral domain divided into simplexes: (a) the vertexes of each surface of a rigid block are stored in clockwise order; (b) surface I is divided into several trangles; (c) the rigid block is divided into several tetrahedrons according to the surface I

where Ω^e is the integral domain; L_i(i=1,2,3,4) are volume coordinates of the tetrahedrons as shown in Fig. 9(b); V_{1234} is the volume of the integral domain.

The correspondence between volume coordinate L_i and global coordinate (x, y, z) are as follows,

$$\begin{cases} x = L_1x_1 + L_2x_2 + L_3x_3 + L_4x_4 \\ y = L_1y_1 + L_2y_2 + L_3y_3 + L_4y_4 \\ z = L_1z_1 + L_2z_2 + L_3z_3 + L_4z_4 \end{cases} \tag{35}$$

where x_i, y_i, z_i (i=1,2,3,4) are vertex coordinates of the tetrahedron in global system.

4.2 Vertex sorting method for the rigid blocks

Ensuring the vertexes of each surface are stored in sequence is very important for numerical integration in 3-D RBSM. İn this section, an efficient vertex soring method is proposed.

As shown in Fig. 10, the initial storage order of the surface vertexes is *i*, *j*, *k*, *l*, *m*, while the actual vertex order is shown in Fig. 10.

Assuming the storage order of vertex *i* is 1, and selecting the outer normal vector $\vec{n}$ as the reference vector of the surface, the storage order of vertex *j* can be determined by the method shown in Fig. 10. It is easy to find out that the direction of vector $\vec{n}_j$ and $\vec{n}_m$ are consistent with that of the reference vector $\vec{n}$, which indicates that there are two vertexes between vertex *i* and *j*, so that the storage order of vertex *j* is 4.

The storage order of vertex *k* can be determined from Fig. 11, and its order is 3.

The same method can also be applied to determine storage orders of other vertexes on the surface, and the final storage order of the surface vertexes is *i*, *m*, *k*, *j*, *l*.

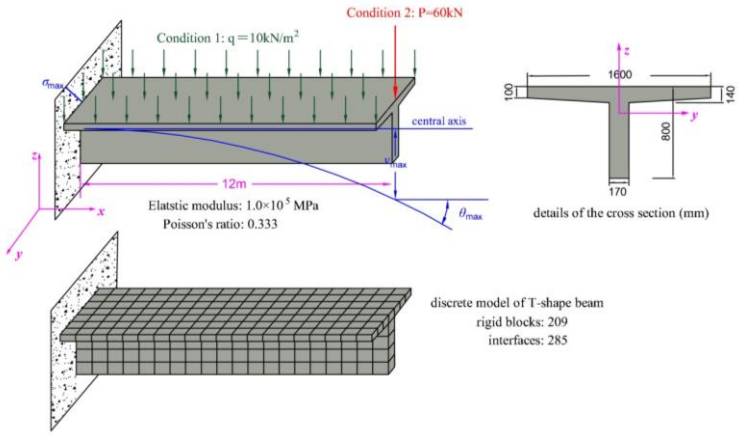

Fig. 13 A elastic cantilever T-shape beam under two different load conditions

4.3 The simplex integration over a complex-shape region

By applying the sorting method, vertexes of each surface are stored in clockwise order, as shown in Fig. 12(a). For surface integration, a surface can be divided into several triangles, as shown in Fig. 12(b), and the point R_p is defined by,

$$\begin{cases} x_{R_P} = \dfrac{x_1 + \cdots + x_i + \cdots + x_{m_{surface}}}{m_{surface}} \\ y_{R_P} = \dfrac{y_1 + \cdots + y_i + \cdots + y_{m_{surface}}}{m_{surface}} \\ z_{R_P} = \dfrac{z_1 + \cdots + z_i + \cdots + z_{m_{surface}}}{m_{surface}} \end{cases} \tag{36}$$

where $m_{surface}$ is the number of vertex composing the surface and x_i, y_i, z_i are their coordinates.

For volume integration, a rigid block will be divided into several tetrahedrons according to the surfaces, as shown in Fig. 12(c), and the point Rv is defined by Eq. (4).

Finally, the surface and volume integration for 3-D RBSM can be conducted by applying simplex integration formula to each unit simplex (triangles for surface integrations and tetrahedrons for volume integrations), and then superposing the results.

4.4 Centroids of rigid blocks

The degrees of freedom of rigid body spring models are defined at the centroid of blocks, but not at the computational point R_V. In order to determine the centroid, a block will be divided into several tetrahedrons by the method described in Fig. 12. For each tetrahedron, the centroid can be determined by,

$$\begin{cases} x_{gi} = \dfrac{x_{1i} + x_{2i} + x_{3i} + x_{4i}}{4} \\ y_{gi} = \dfrac{y_{1i} + y_{2i} + y_{3i} + y_{4i}}{4} \\ z_{gi} = \dfrac{z_{1i} + z_{2i} + z_{3i} + z_{4i}}{4} \end{cases} \tag{37}$$

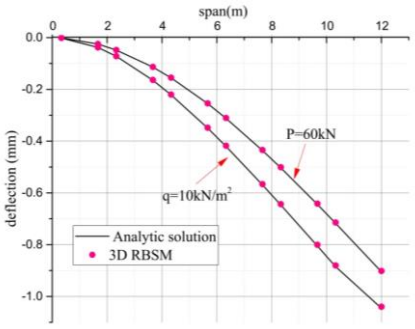

Fig. 14 The deflection of the cantilever T-shape beam

Table 1 Comparison between analytic solution and numerical solution

Item	Load condition 1			Load condition 2		
	RBSM solution	Analytic solution	Error	RBSM solution	Analytic solution	Error
v_{max} (mm)	-1.081	-1.086	0.46%	-0.901	-0.905	0.44%
θ_{max} (rad)	0.119	0.121	1.65%	0.110	0.113	2.65%
σ_{max} (MPa)	0.263	0.264	0.38%	0.198	0.198	0.00%

*v_{max}, θ_{max}: The maximum displacements; σ_{max}: The maximum normal stress value

where x_{1i}, y_{1i}, z_{1i}, …, x_{4i}, y_{4i}, z_{4i} are the vertex coordinates of tetrahedron i.

The volume of each tetrahedron is

$$V_i = \frac{1}{6}\det\begin{vmatrix} 1 & x_{1i} & y_{1i} & z_{1i} \\ 1 & x_{2i} & y_{2i} & z_{2i} \\ 1 & x_{3i} & y_{3i} & z_{3i} \\ 1 & x_{4i} & y_{4i} & z_{4i} \end{vmatrix} \tag{38}$$

The centroid coordinates of the block can be determined by,

$$\begin{cases} x_g = \left(\sum_1^n x_{gi} V_i\right) \Big/ \sum_1^n V_i \\ y_g = \left(\sum_1^n y_{gi} V_i\right) \Big/ \sum_1^n V_i \\ z_g = \left(\sum_1^n z_{gi} V_i\right) \Big/ \sum_1^n V_i \end{cases} \tag{39}$$

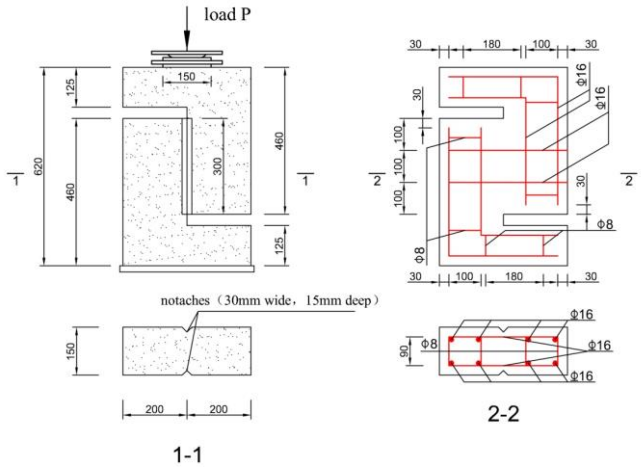

Fig. 15 Geometry details and reinforcement arrangement of the Z-shape component (mm)

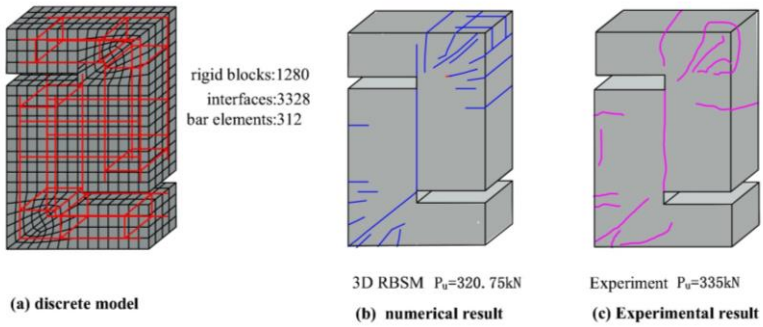

Fig. 16 Result comparison of the 3-D RBSM and the experiment: (a) discrete model of the Z-shape component; (b) crack patterns predicted by the proposed RBSM; (c) crack patterns obtained the experimental test

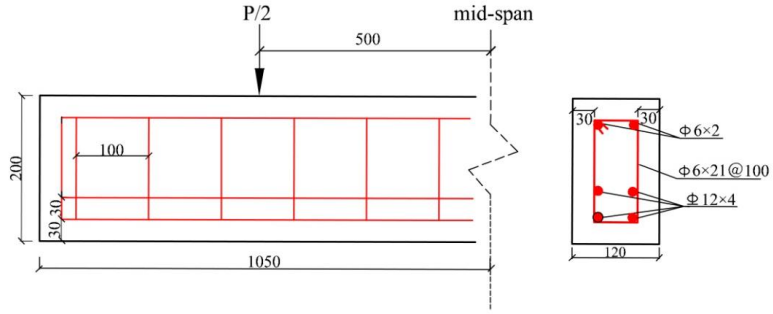

Fig. 17 Geometry Details and reinforcement arrangement of the test beam (mm)

Table 2 Parameters of concrete and reinforcement

f_t/MPa	f_c/MPa	E_{c0}/GPa	λ_0	λ_f	c/MPa	φ	f_y/MPa	f_u/MPa	E_{s0}/GPa	ε_u	G_f/(N/m)
2.64	49.4	32.5	0.20	0.36	5.1	62.5°	360.2	568.1	200	0.075	100

where n is the number of tetrahedrons composing the block.

5. Presentation of studied cases

5.1 Case 1

To verify the accuracy of the proposed method, an elastic cantilever T-shape beam under different load conditions is studied, as shown in Fig. 13. The comparison between the analytic solution and numerical solution is shown in Table 1. The deflection of the beam is presented in Fig. 14.

It is noticeable that the overall error of the proposed method is less than 2.65%, and the stress error is less than 1%.

5.2 Case 2

In order to indentify the performance of the proposed method in direct-shear failure, numerical results of the proposed method must be compared with the actual experimental data. Based on the experimental results of the reinforcement concrete specimen (as shown in Fig. 15)

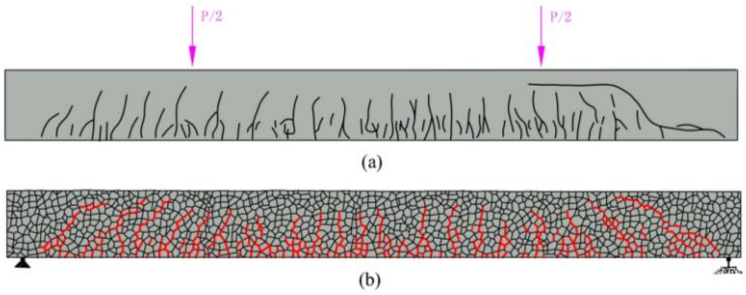

Fig. 18 Crack distribution obtained by different methods: (a) experiment; (b) the 3-D rigid body spring method

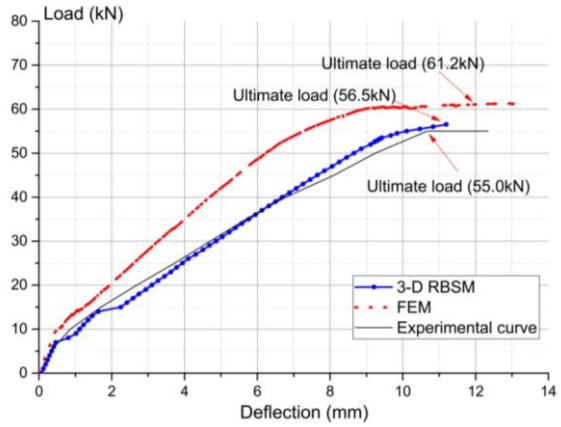

Fig. 19 The load-deflection curves of the test beam

under push-off test program (Zhang 2009), a 3-D rigid body spring model is developed for the experimental specimen, as shown in Fig. 16(a). The steel bars are modeled by a series of regular bar elements and the bonding properties between the concrete and the reinforcing steel are introduced by special linkage elements proposed in this paper. The boundary conditions are achieved by restraining the DOFs of the corresponding blocks. The material properties of the concrete and reinforcement adopted in the model are listed in Table 2. The step-by-step search method is adopted to approach the ultimate bearing capacity of the beam. When the load reaches 320.75 kN, shear cracks at the notches fully developed, and steel bars yielded. The cracks patterns predicted by the proposed method and the push-off test are shown in Figs. 16(b)-(c).

The comparison result of Figs. 16(b)-(c) shows that the crack distributions and the ultimate load P_u of the test specimen predicted by the proposed method are in good agreement with the experimental results.

5.3 Case 3

To further check the performance of the proposed model in a bending-shear failure process analysis, an RC simple-supported beam under two points of load is adopted herein and corresponding experiment is conducted in our laboratory. The test beam has a cross section of 200 mm by 120 mm with a clear span of 2000 mm, and the arrangements of steel bars are shown in Fig. 17. A stepped loading mode is adopted, and when the experimental load reaches 10 kN, vertical cracks appear at the bottom of the beam. After that, vertical cracks continue developing. When the load reaches 40 kN, obvious diagonal cracks appear in the bending shear regions. When the load exceeds 55 kN, the beam fails and the crack pattern is shown in Fig. 18(a). During the loading process, the vertical deflection is measured using the dial gauge at the mid-span where the maximum deflection is predicted, and the load–deflection curve is shown in Fig. 19.

Table 3 Material properties adopted in numerical models

f_t/MPa	f_c/MPa	E_{c0}/GPa	λ_0	λ_f	c/MPa	φ	f_y/MPa	f_u/MPa	E_{s0}/GPa	ε_u	G_f/(N/m)
2.2	23.4	31.5	0.20	0.42	4.5	62.5°	235	355	20	0.075	100

A 3D rigid body spring model based on Voronoi diagram is developed for the experimental beam, as shown in Fig. 20. By using the Voronoi diagram, the concrete material is partitioned into a collection of rigid blocks with random geometry. Reinforcement is modeled by a series of regular bar elements and the bonding properties between the concrete and the reinforcing steel are introduced by special linkage elements proposed in this paper. The boundary conditions can be achieved by restraining the DOFs of the corresponding blocks. The material properties of the concrete and reinforcement adopted in the model are listed in Table 3. The step-by-step search method is adopted to approach the ultimate bearing capacity of the beam. When the load reaches 8 kN, vertical cracks appear at the bottom of the beam. When the load reaches 35 kN, obvious diagonal cracks appear in the bending shear regions. The final convergence load is 56.5 kN, and the crack patterns are shown in Fig. 18(b). The load-deflection curve is shown in Fig. 19.

For comparison, a finite element model (FEM) is developed for the test beam using the ABAQUS program, which has been widely used in both engineering and academic areas to predict complicated behavior of RC structures with high credibility (Demir and Husem 2015). In the present work, eight-node solid elements (C3D8R) are used to model the concrete, and internal reinforcement is modeled by 3-D truss elements (T3D2). The FEM model consists of 2115 nodes, 1986 concrete elements and 546 reinforcement elements, as shown in Fig. 21. The plastic damage constitutive model is adopted to simulate the nonlinear behavior of concrete under compression and tension, and steel bars are assumed to be a bilinear elastic material model as shown in Fig. 7(a). The bond-slip effect between the concrete and internal reinforcement is modeled by spring elements. Basic material properties for the

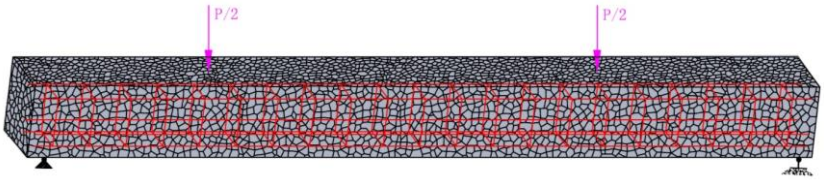

Fig. 20 3-D RBSM model of the experimental beam

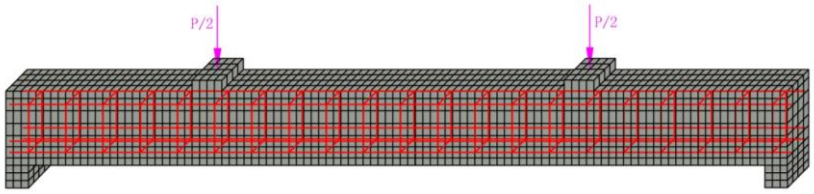

Fig. 21 The finite element model of the experimental beam

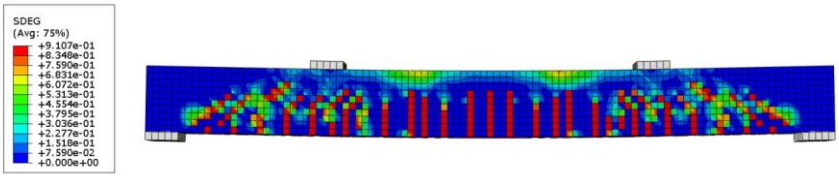

Fig. 22 The field output of scalar stiffness degradation of the test beam (FEM)

concrete and steel reinforcement are listed in Table 3. The load-deflection response of the test beam predicted by the finite element model is plotted with the RBSM and experimental results in Fig. 19, and the field output of scalar stiffness degradation is shown in Fig. 22.

The ultimate loads and load-deflection curves of the test beam from the proposed method, experiment and FEM are close to each other as shown in Fig. 19.

The comparison results of Figs. 18(a)-(b) shows that the crack characteristics of the test beam, such as location, height and development trend, predicted by the proposed method are in good agreement with the experimental results.

The crack distribution can be roughly predicted from the field output of scalar stiffness degradation of the finite element model (As shown in Fig. 23), but there is a certain deviation from the experimental results.

6. Conclusions

This paper has presented a practical, computationlly efficient method for simulating the failure process of reinforced concrete structures. In the proposed model, concrete, reinforcing steels, and their interfaces are represented as discrete entities. Concrete is partitioned into a collection of rigid blocks, and a uniform distribution of normal and tangential springs along their boundaries is defined to reflect the material properties of concrete. Reinforcing material is explicitly modeled by a regular bar element and special linkage element. Integral calculation on complex-shape region is a key problem of three-dimensional RBSM, and an efficient and accurate integral method is proposed in this paper. The applicability and effectiveness of the proposed method is firstly confirmed by the elastic analysis of a cantilever T-shape beam, and then it was applied to analyze the failure processes of a Z-type component under direct shear loading and a RC beam under two-point loading. The following conclusions are led through this research:

• The proposed 3-D RBSM can successfully predict the load-deformation response, ultimate strengths, failure mechanisms, and cracking patterns of reinforced concrete components. Crack initiation and propagation of concrete are presented realistically. That is, the proposed method can simulate cracking behavior realistically;

• Mesh construction in the proposed method is greatly facilitated. Random geometry models based on the Voronoi diagram greatly reduce mesh bias on potential crack directions, and crack trajectories need not to be anticipated;

• An accurate numerical integral method is proposed in this paper to carry out the integration on complex 3-D domain, and numerical results prove that the method is feasible and efficient;

• The proposed method provides with a simple framework for automatically introducing reinforcing material. Reinforcing steel can be freely positioned in the structural domain and irrespective of the mesh geometry of concrete. Since model preprocessing efforts are greatly reduced, the approach can be applied as a practical means for integrating analyses and design process in reinforced concrete structures.

Acknowledgments

The research described in this paper is financially supported by the Natural Science Foundation of China (51678253, 41472259) and National Key Research and

Develop Program of China (2016YFC080250504). These supports are gratefully acknowledged.

References

Belytschko, T. and Black, T. (1999), "Elastic crack growth in finite elements with minimal remeshing", *J. Numer. Meth. Eng.*, **45**, 601-620.

Bernardi, P., Cerioni, R., Michelini, E. and Sirico, A. (2016), "Numerical modelling of the cracking behaviour of RC and SFRC shear-critical beams", *Eng. Fract. Mech.*, **167**, 151-166.

Bolander, J.E., Hong, G.S. and Yoshitake, K. (2000), "Structural concrete analysis using rigid-body-spring networks", *Comput.-Aid. Civil Infrastruct. Eng.*, **15**, 120-133.

Bolander, J.E. and Saito, S. (1998), "Fracture analyses using spring networks with random geometry", *Eng. Fract. Mech.*, **61**, 569-591.

Burns, S.J. and Hanley, K.J. (2017), "Establishing stable time-steps for DEM simulations of non-collinear planar collisions with linear contact laws", *J. Numer. Meth. Eng.*, **110**, 186-200.

Carter, B., Wawrzynek, P. and Ingraffea, A. (2000), "Automated 3-D crack growth simulation", *J. Numer. Meth. Eng.*, **47**, 229-253.

Comite Euro-international du Beton (1990), *CEB-FIB Model Code 1990 First Draft*, CEB, Pair, France.

Demir, S. and Husem, M. (2015), "Investigation of bond-slip modelling methods used in FE analysis of RC members", *Struct. Eng. Mech.*, **56**(2), 275-291.

Gedik, Y.H., Nakamura, H., Yamamoto, H. and Kunieda, M. (2011), "Evaluation of three-dimensional effects in short deep bemas using a rigid-body-spring-model", *Cement Concrete Compos.*, **33**(9), 978-991.

Gu, X.L., Hong, L., Wang, Z.L. and Lin, F. (2013), "A modified rigid-body-spring concrete model for prediction of initial defects and aggregates distribution effect on behavior of concrete", *Comput. Mater. Sci.*, **77**, 355-365.

Guo, N. and Zhao, J.D. (2014), "A coupled FEM/DEM approach for hierarchical multiscale modelling of franular media", *J. Numer. Meth. Eng.*, **99**, 789-818.

Hariri-Ardebili, M.A. and Seyed-Kolbadi, S.M. (2015), "Seismic cracking and instability of concrete dams: Smeared crack approach", *Eng. Fail. Analy.*, **52**, 45-60.

Jiang, S.Y. and Du, C.B. (2017), "Study on dynamic interaction between crack and inclusion or void by using XFEM", *Struct. Eng. Mech.*, **63**(3), 669-681.

Kara, I.F., Ashour, A.F. and Dundar, C. (2017), "Analysis of R/C frames considering cracking effect and plastic hinge formation", *Struct. Eng. Mech.*, **63**(5), 669-681.

Kawai, T. (1977), "New element models in discrete structural analysis", *J. Soc. Nav. Archit. Jap.*, **141**, 187-193.

Li, M.G., Yu, H.T. and Wang, J.H. (2015), "A multiscale coupling approach between discrete element method and finite difference method for dynamic analysis", *J. Numer. Meth. Eng.*, **102**, 1-21.

Murthy, A.R. and Priya, D.S. (2017), "Weibull distribution based constitutive model for nonlinear analysis of RC beams", *Struct. Eng. Mech.*, **61**(4), 463-473.

NandaKumar, M.R., Murthy, A.R. and Gopinath, S. (2016), "XFEM for fatigue analysis of cracked stiffened pannels", *Struct. Eng. Mech.*, **57**(1), 65-89.

Ors, D.M.F., Okail, H.O. and Zaher, A.H. (2016), "Modeling of shear deficient beams by the mixed smeared/discrete cracking approach", *Hous. Build. Nat. Res. Cent.*, **12**(2), 123-136.

Saito, S. and Hikosaka, H. (1999), "Numerical analyses of reinforced concrete structures using spring network models", *J. Mater. Concrete Struct. Pave.*, **44**, 289-303.

Shi, G.H. (1988), "Discontinuous deformation analysis: A new numerical model for the statics and dynamics of block systems", Ph.D. Dissertation, University of California at Berkeley, Berkeley, U.S.A.

Shi, G.H. (1994), "Modeling dynamic rock failure by discontinuous deformation analysis with simplex integrations", *Proceedings of the 1st North American Rock Mechanics Symposium*, Austin, Texas, U.S.A., July.

Wang, J.W., Zhu, H. and Wang, H. (2002), "Equivalent uniaxial constitutive model of concrete in plane strain", *J. Hohai Univ.*, **30**, 6-10.

Yao, C., Jiang, Q.H. and Shao, J.F. (2015), "Numerical simulation of damage and failure in brittle rocks using a modified rigid block spring method", *Comput. Geotech.*, **64**, 48-60.

Yao, C., Shao, J.F., Jiang, Q.H, and Zhou, C.B. (2017), "Numerical study of excavation induced fractures using an extended rigid block spring method", *Comput. Geotech.*, **85**, 368-383.

Zhang, Q., Wang, Z.Q. and Xia, X.Z. (2012), "Interface stress element method and its application in analysis of anti-sliding stability of gravity dam", *Sci. Chin. Technol. Sci.*, **55**, 3285-3291.

Zhang, S. (2009). "Analysis of the ultimate load of one-plane prestressing concrete box girder tied arch bridge", Ph.D. Dissertation, Dalian University of Technology, Dalian, China.

Zhang, X. (1999), "Slope stability analysis based on the rigid finite element method", *Geotech.*, **49**, 585-593.

CC